The Astrophysical Journal Supplement Series, 241:35 (20pp), 2019 April https://doi.org/10.3847/1538-4365/ab0825

The Period–Luminosity Relations of Red Supergiants in M33 and M31

Yi Ren[1], Bi-Wei Jiang[1], Ming Yang[2], and Jian Gao[1]
[1] Department of Astronomy, Beijing Normal University, Beijing 100875, People's Republic of China; bjiang@bnu.edu.cn
[2] Institute for Astronomy, Astrophysics, Space Applications & Remote Sensing, National Observatory of Athens, Vas. Pavlou and I. Metaxa, Penteli 15236, Greece
Received 2018 December 2; revised 2019 January 31; accepted 2019 February 15; published 2019 April 16

Abstract

Based on previously selected preliminary samples of red supergiants (RSGs) in M33 and M31, the foreground stars and luminous asymptotic giant branch stars are further excluded, which leads to the samples of 717 RSGs in M33 and 420 RSGs in M31. With the time-series data from the Intermediate Palomar Transient Factory survey spanning nearly 2000 days, the period and amplitude of RSGs are analyzed. According to the light-curve characteristics, they are classified into four categories in which 84 and 56 objects in M33 and M31, respectively, are semi-regular variables. For these semi-regular variables, the pulsation mode is identified by comparing with the theoretical model, which yielded 19 (7) sources in the first overtone mode in M33 (M31), and the other 65 (49) RSGs in M33 (M31) in the fundamental mode. The period–luminosity (P–L) relation is analyzed for the RSGs in the fundamental mode. The P–L relation is found to be tight in the infrared, i.e., the Two Mircon All-Sky Survey (2MASS) JHK_S bands and the short-wavelength bands of *Spitzer*. Meanwhile, the inhomogeneous extinction causes the P–L relation scattering in the V band, and the dust emission causes the less tight P–L relation in the *Spitzer*/[8.0] and [24] bands. The derived P–L relations in the 2MASS/K_S band are in agreement with those of RSGs in the Small Magellanic Cloud, the Large Magellanic Cloud, and the Milky Way within the uncertainty range. It is found that the number ratio of RSGs pulsating in the fundamental mode to the first overtone mode increases with metallicity.

Key words: stars: late-type – stars: oscillations (including pulsations) – supergiants

Supporting material: extended figures, machine-readable tables

1. Introduction

Red supergiants (RSGs) are Population I stars in the helium burning stage with a mass range of about 9–27 $M_\odot$. They have relatively low effective temperatures of ∼3000–4000 K and the corresponding spectral types of late K to M types (Massey et al. 2008). Their radius is large, with the maximum radius being $\sim 1500 R_\odot$ (Levesque et al. 2005), so that they have low surface gravity of $\log g < 1.0$ but high luminosity of ~ 3500–$630{,}000 L_\odot$ (Massey et al. 2008; Massey & Evans 2016).

RSG is a phase of very significant mass loss (Stothers & Chin 1996). The Reimers law (Reimers 1975; Kudritzki & Reimers 1978) is an empirical relation between the mass-loss rate (MLR), stellar luminosity, radius, and mass derived from a sample of red giants and RSGs: $\dot{M} = 5.5 * 10^{-13} L_\odot R_\odot / M_\odot$. van Loon et al. (2005) also derived the relationship between MLR and stellar parameters, but based on the samples of RSGs and oxygen-rich asymptotic giant branch stars (AGBs) in the Large Magellanic Cloud (LMC), $\log(\dot{M}) = -5.5 + 1.05 \log(L/10{,}000 L_\odot) - 6.3 \log(T_{\rm eff}/3500\,{\rm K})$. However, Mauron & Josselin (2011) pointed out that the result might be biased toward larger values of $\dot{M}$ because the samples contained mainly extremely dusty RSG stars and the limitations of the mid-infrared data available then.

Circumstellar dust forms with stellar mass loss, and most RSGs have some amount of circumstellar dust (Verhoelst et al. 2009). These dust have obvious infrared emission, especially in the mid-infrared band, which makes the luminosity of such RSGs in the infrared band exceed the upper limit of the theoretical luminosity of RSGs, and the contribution can be observed in the *Spitzer* 8 and 24 μm band.

RSGs are critical and important as both direct and indirect progenitors of supernovae (SNe) that spend some time in the RSG phase. Lower mass RSGs are known to be the direct progenitors of core-collapse SNe II-P with clear hydrogen lines in the optical spectrum and a distinctive plateau in visual light curves. A certain number of SNe II-P have been proved to associate with RSG progenitors by observation (Smartt 2015; Maund 2017). However, higher-mass RSGs, first noticed by Smartt et al. (2009), have not been detected as SN progenitors. This may indicate that higher-mass RSGs are not the direct progenitors of an SN; instead, they evolve back across the Hertzsprung–Russell (H–R) diagram, spending a short time as yellow supergiants (YSGs), blue supergiants, or Wolf-Rayet stars before exploding as SNe (Ekström et al. 2012). But high-mass RSGs play an important role in their final fate because the mass-loss processes and dust production in the RSG phase will influence their ending.

A large amount of dust is detected in high-redshift galaxies when the low-mass stars have not evolved to the AGB phase to become the dust contributor (Riechers et al. 2013). Therefore, the massive stars are the main, if not unique, providers of dust then. RSGs and SNe must be the major contributors to the interstellar dust in such distant galaxies.

Most RSGs show some degree of variability in the visual band. The typical amplitude of variation in the V band is about 1 mag, while in the near-infrared the amplitude is smaller, about 0.25 mag in the K band, and even smaller in the mid-infrared band (Levesque et al. 2007; Yang et al. 2018). According to the characteristics of light variation, the RSG variability is divided into two categories: one is irregular variation that is too complex to be delineated by any period, the

other is semi-regular variation that can be further divided into two subclasses: one with short period ($\leqslant$several hundred days) and the other with a long secondary period (LSP, $\geqslant$thousand days). The main difficulty in the study of variability of RSGs is the long timescale of variation. The time-series data need to span over several hundreds of days to cover at least one entire period of variation. If the LSP is present and desired to be determined, an even longer time baseline is required to last for several years.

Like other types of pulsating variables, RSGs exhibit the period–luminosity (P–L) relation. Both the theory and observation prove the existence of the P–L relation in RSGs with semi-regular variation, especially the RSGs with short period variation. Guo & Li (2002) derived the theoretical P–L relations of fundamental (FU), first overtone (1O) and second overtone pulsation models for 15–30 $M_{\odot}$ RSGs. In the Milky Way, based on the light curves collected by the American Association of Variable Star Observers (AAVSO) with a span of 60 yr, Kiss et al. (2006) studied 18 red supergiant stars to obtain their P–L relation.

Based mainly on the All Sky Automated Survey (ASAS; Pojmanski 2002) and MAssive Compact Halo Objects (MACHO; Alcock et al. 1997) observation, Yang & Jiang (2011, 2012) analyzed the light curves of 112 RSGs in the Small Magellanic Cloud (SMC) and 169 RSGs in the LMC and determined the periods of those semi-regular variables. They derived the P–L relation based on 47 RSGs in the LMC and 21 RSGs in the SMC with short period semi-regular variation, which was consistent with the result of the theory (Guo & Li 2002). They also analyzed a sample of 40 RSGs in M33 and obtained their P–L relation in the Two Mircon All-Sky Survey (2MASS)/K_S band using the period from Kinman et al. (1987).

An extension to the environments of various metallicity will examine its effect on the P–L relationship. In the Local Group, the metallicity has a wide range from sub-solar in the SMC ($12 + \log(\mathrm{O/H}) = 8.13$; Russell & Dopita 1990) and LMC ($12 + \log(\mathrm{O/H}) = 8.37$; Russell & Dopita 1990) to solar in the Milky Way ($12 + \log(\mathrm{O/H}) = 8.70$; Esteban & Peimbert 1995) and M33 ($12 + \log(\mathrm{O/H}) = 8.75$; Garnett et al. 1997) and then to super-solar in M31 ($12 + \log(\mathrm{O/H}) = 9.00$; Zaritsky et al. 1994). The metallicity is known to affect the ratios of blue-to-red supergiants (B/R) and Wolf-Rayet stars to RSGs (W-R/RSG). The B/R ratio changes by about seven times (Maeder et al. 1980) and the W-R/RSG ratio changes by about 100 times over 0.9 dex in metallicity (Massey 2002). Unfortunately, differences in the W-R/RSG ratio cannot be fully explained by stellar evolutionary models of massive stars. Besides, metallicity has an obvious impact on color indices (or spectral types) and effective temperatures of RSGs. The spectral types of RSGs shift to earlier at lower metallicities (Elias et al. 1985; Massey & Olsen 2003; Levesque & Massey 2012; Dorda et al. 2016). The effective temperatures of RSGs shift to warmer at lower metallicities, which was demonstrated by observation in different regions of M33 (Drout et al. 2012). The effect of metallicity on the P–L relation of RSGs is, however, not yet clear. From the studies of the variability of RSGs in the SMC, the LMC, and the Milky Way, the P–L relations seem to be very similar despite of various metallicity. From the evolution and pulsation model of RSGs, for a given period, the higher the metallicity is, the fainter the luminosity is. The luminosity increases by 0.25 mag while metal abundance is doubled at a given period. On the other hand, the P–L relations at different metallicities show a tendency of an increasing period with metal abundance (Guo & Li 2002).

Now, the Intermediate Palomar Transient Factory (iPTF) survey (Law et al. 2009; Rau et al. 2009) covers the M33 and M31 sky areas, and its time baseline is about 2000 days, providing the possibility for an elaborate analysis of the variation of RSGs in M33 and M31. Soraisam et al. (2018) already analyzed the P–L relation of RSG in M31 using iPTF data spanning from MJD 56,000 to 58,000. Here, we analyze the case of M33. For consistency, M31 data is also included, and we checked the agreement with the result of Soraisam et al. (2018).

2. The Sample of RSGs

2.1. Foreground Stars

A complete and pure sample of RSGs forms the solid basis to obtain a reliable P–L relation. Spectroscopy is the best tool to identify RSGs in the Milky Way. Unfortunately, the extragalactic RSGs may not be bright enough for a high signal-to-noise ratio spectrum. On the other hand, they benefit from the advantage of being at almost the same distance so that the apparent magnitude plays a role like absolute magnitude. Therefore, RSGs in the extragalactic systems can be identified by multiband photometry (e.g., Massey et al. 2006). The threshold of the luminosity and the range of color indexes are used to select the RSG candidates. For example, the $V = 20$ mag cutoff and the color index $V - R \geqslant 0.85$ are used to select the RSG candidates in M31 (Massey et al. 2009; Massey & Evans 2016), where the $V = 20$ mag cutoff ensures sufficient brightness to block out the AGBs and the color index $V - R \geqslant 0.85$ restricts the stars to a K and later type. The sample selected by this method can still be contaminated by foreground dwarf stars and red giants in the Galactic halo. Massey (1998) proved that the combination of color indexes $V - R$ and $B - V$ can effectively separate RSGs from the foreground dwarfs, because $V - R$ is only sensitive to the effective temperature, while $B - V$ is sensitive to both the effective temperature and surface gravity so that the low surface gravity RSGs and the high surface gravity dwarfs are significantly different in $B - V$. Comparison of the Besançon model (Robin et al. 2003) with the observed color–magnitude diagram (CMD; Massey et al. 2016) and the kinetic identification (comparing the radial velocities of RSGs (Massey et al. 2009) with the H II regions in M31 (Rubin & Ford 1970)) found that the pollution probability of red giants in the Galactic halo was rather small.

The Local Group Galaxies Survey (LGGS; Massey et al. 2006, 2007) took images of several galaxies in the Local Group, including M33 and M31, using the 4 m telescopes at the Kitt Peak National Observatory and the Cerro Tololo Inter-American Observatory. This survey worked in multiple bands (U, B, V, R, and I) at a 1 $\sim$ 2% photometry precision with a limiting magnitude of $\sim$21 mag. Massey et al. (2009) and Massey & Evans (2016) published a sample of 437 RSG candidates in M31 based on the two-color diagrams (TCD) method. We select RSG candidates in M33 by the same method with the criteria of $V < 20$, $V - R > 0.65$, and $B - V > -1.599(V - R)^2 + 4.18(V - R) - 0.83$ (see Drout et al. 2012) and obtain a sample of 749 RSG candidates in Figure 1. Significant differences are seen to show up between

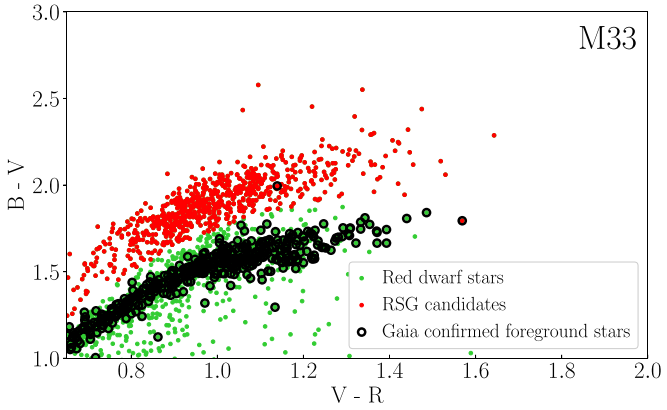

Figure 1. $B-V/V-R$ TCD of all red stars in M33. Foreground red dwarfs are marked as green dots, RSG candidates are marked as red dots, and foreground stars confirmed by *Gaia* are marked as black circles.

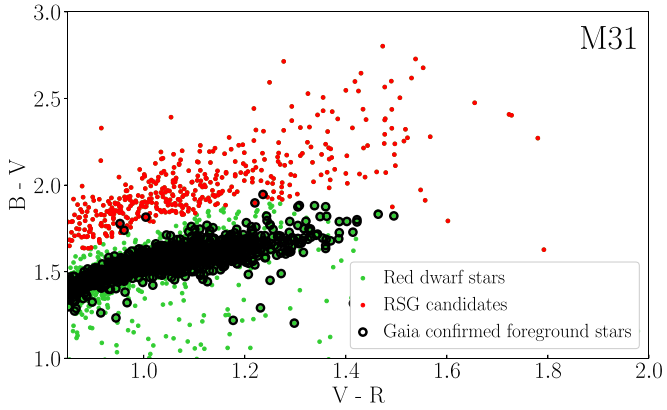

Figure 2. $B-V/V-R$ TCD of all red stars in M31. Foreground red dwarfs are marked as green dots, RSG candidates are marked as red dots, and foreground stars confirmed by *Gaia* are marked as black circles.

supergiant candidates and foreground dwarfs that locate above and below the separating line, respectively.

Although Massey et al. (2009, 2016) demonstrate that the pollution probability of foreground red giants is small, we further use the distance of stars to check this argument directly with the help of the *Gaia* data release 2 (DR2) that provides parallaxes of 1.3 billion stars (Gaia Collaboration et al. 2018). All stars shown in Figures 1 and 2 are cross-matched with the *Gaia* DR2, and their distances are calculated with the Smith-Eichhorn correction method (Smith & Eichhorn 1996) from the *Gaia*-measured parallax. The distances of 918 red stars in M33 and 2216 red stars in M31 have relative error better than 20%. Two (five) RSG candidates in M33 (M31) selected by the TCD method are found to have a distance modulus less than 24.66 (24.40)—the distance modulus of M33 (M31) and are marked by black circles in Figures 1 and 2. This confirmed that the pollution probability of red giants is truly small, on the scale of about 1%. Besides, foreground stars from the TCD method are analyzed to check the agreement with *Gaia* distances: 430 of 1677 foreground stars in M33 and 1161 of 3589 foreground stars in M31 are confirmed by the *Gaia* distances. Removing the foreground red giants from the TCD-selected samples, we are left with the samples of 747 RSG candidates in M33 and 432 RSG candidates in M31, consequently.

2.2. The AGB Stars

Once the foreground stars are removed, the only pollution is the AGB stars in M33 and M31. On the H–R diagram, the high-luminosity AGB stars have a definite overlap with the low-luminosity RSGs (Brunish et al. 1986). We solve this problem by setting the luminosity threshold in multiple bands. According to the mass–luminosity relation of massive stars:

$$\frac{L}{L_{\odot}} = \left(\frac{M}{M_{\odot}}\right)^{\gamma},$$

where $\gamma \approx 4$ (Stothers & Leung 1971), and the RSG luminosity corresponding to the mass range of 9–27 $M_{\odot}$ is 9^4–27^4 $L_{\odot}$. With the relationship between luminosity and absolute bolometric magnitude,

$$M_{\rm bol} = 4.74 - 2.5 \times \log\left(\frac{L}{L_{\odot}}\right),$$

Table 1
Linear Fit Results between the Bolometric Magnitude and the Multiband Magnitude from RSG Candidates in M33

Band	Slope	Intercept	Correlation	$m_{\rm max}$	$m_{\rm min}$
J	1.09	−2.90	0.95	13.54	18.73
H	1.09	−3.71	0.94	12.73	17.93
$K_{\rm S}$	1.15	−5.13	0.97	12.28	17.79
[3.6]	1.25	−6.80	0.86	12.02	17.97
[4.5]	1.32	−7.87	0.85	12.06	18.36
[5.8]	1.41	−9.75	0.79	11.46	18.17
[8.0]	1.34	−9.57	0.58	10.61	16.99
[24]	1.09	−7.55	0.45	8.84	14.02

Note. The fitting form follows $m(\lambda) = a * m_{\rm bol}(\lambda) + b$.

the upper and lower limits of $M_{\rm bol}$ are $M_{\rm bol}^{\rm max} = -9.57$ and $M_{\rm bol}^{\rm min} = -4.80$. Given the distance modulus of M33 being 24.66 (Orosz et al. 2007) and of M31 being 24.40 (Perina et al. 2009), the limits of apparent bolometric magnitudes become $m_{\rm bol}^{\rm max} = 15.09$ and $m_{\rm bol}^{\rm min} = 19.86$ for M33 and $m_{\rm bol}^{\rm max} = 14.83$ and $m_{\rm bol}^{\rm min} = 19.60$ for M31. On the observational side, the bolometric K correction in the K band from Bessell et al. (1998a, 1998b) is added to obtain the apparent bolometric magnitude from the apparent K band for the RSG stars within a given mass range. First, the effective temperature is derived from the intrinsic color index $(V-K)_0$: $T_{\rm eff} = 8130.9 - 2113.22(V-K)_0 + 327.883(V-K)_0^2 - 17.7886(V-K)_0^3$, where $(V-K)_0$ is calculated from the observed color by subtracting the interstellar extinction by assuming $A_V = 1$ and $A_K/A_V = 0.12$ for all RSG candidates (Massey & Evans 2016). Then, the bolometric correction in the K band is calculated from $\mathrm{BC}_K = 7.149 - 1.5924(T_{\rm eff}/1000\,\mathrm{K}) + 0.10956(T_{\rm eff}/1000\,\mathrm{K})^2$ (Bessell et al. 1998a, 1998b) where the difference between the K and $K_{\rm S}$ bands is very small and ignored in this work. The linear relationship of the apparent magnitude with the apparent bolometric magnitude is derived, which is used to convert the limits of bolometric magnitudes to that in the corresponding band. The results of the linear fitting between the bolometric magnitude and that in the λ band are shown in Table 1 and Figures 3 and 4, e.g., the upper and lower limits in the J band are derived to be 13.54 and 18.73 mag, which correspond to the limits of apparent

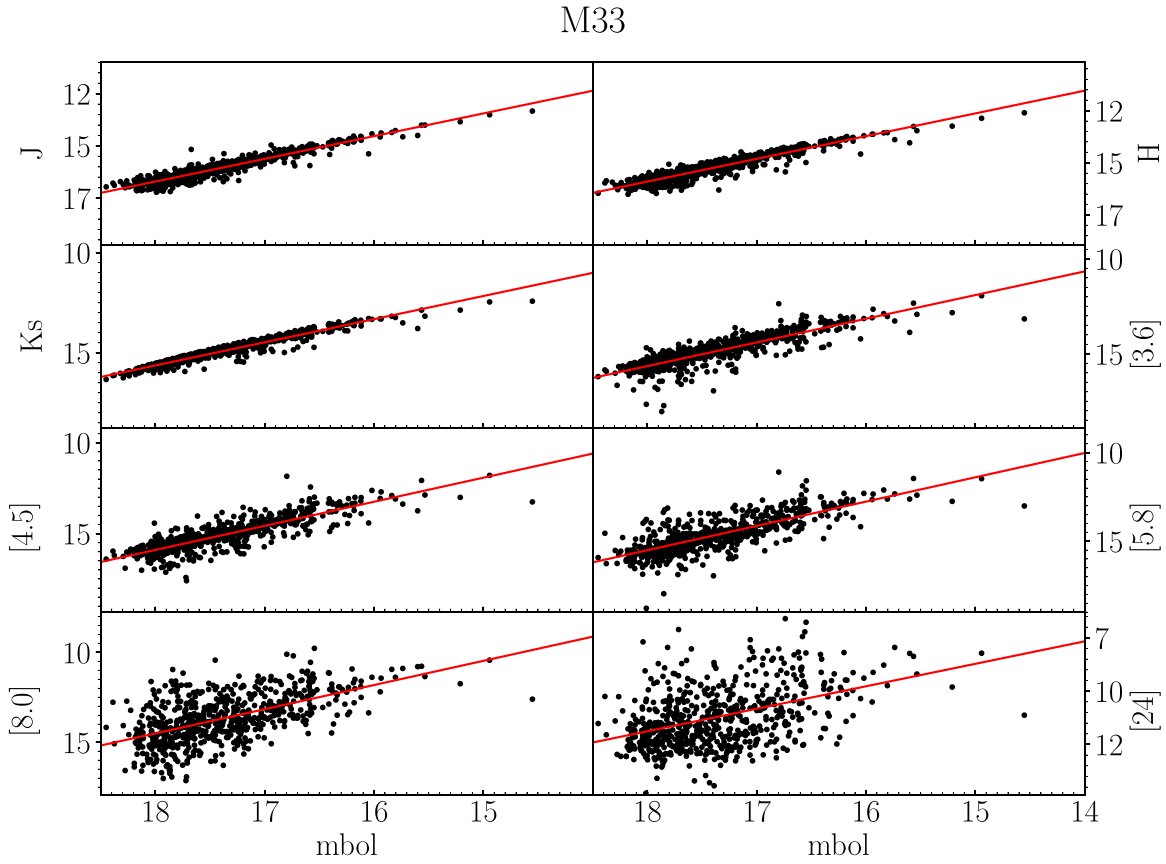

Figure 3. Linear fit between the bolometric magnitude and the multiband magnitude from RSG candidates in M33.

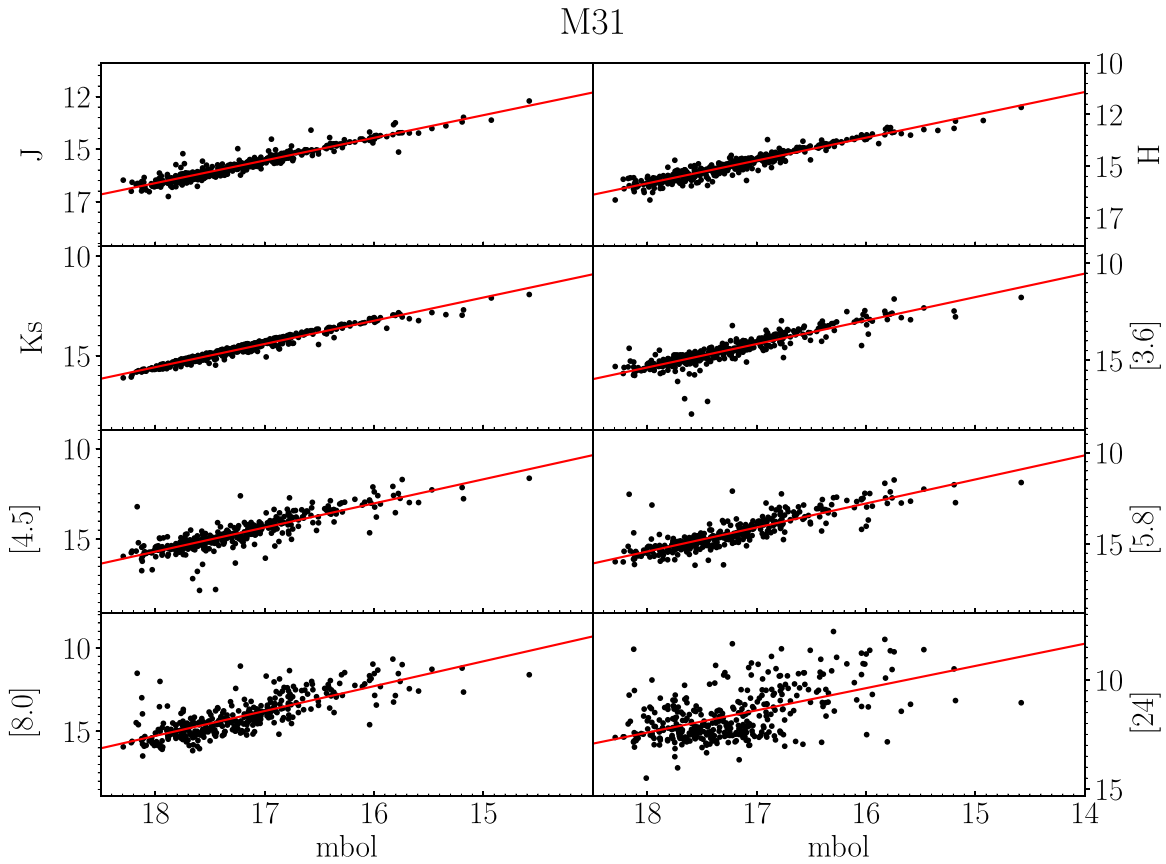

Figure 4. Linear fit between the bolometric magnitude and the multiband magnitude from RSG candidates in M31.

Table 2
Linear Fit Results between the Bolometric Magnitude and the Multiband Magnitude from RSG Candidates in M31

Band	Slope	Intercept	Correlation	$m_{\max}$	$m_{\min}$
J	1.08	−2.85	0.95	13.19	18.35
H	1.11	−4.08	0.95	12.33	17.61
K_S	1.17	−5.43	0.98	11.88	17.45
[3.6]	1.19	−6.10	0.88	11.58	17.27
[4.5]	1.32	−8.01	0.85	11.51	17.79
[5.8]	1.30	−7.99	0.85	11.29	17.49
[8.0]	1.48	−11.41	0.78	10.58	17.66
[24]	1.01	−5.73	0.53	9.22	14.03

Note. The fitting form follows $m(\lambda) = a * m_{\rm bol}(\lambda) + b$.

bolometric magnitudes of $m_{\rm bol}^{\rm max} = 15.09$ and $m_{\rm bol}^{\rm min} = 19.86$ for M33. The case of M31 is presented in Table 2 and Figure 4.

It is worth noting that the linear fitting has a relatively large dispersion in the *Spitzer* 8 and 24 μm bands. This can be understood by the contribution of circumstellar dust to the flux at 8 and 24 μm in addition to the stellar photosphere. This scattering leads to relatively uncertain limits of brightness in the 8 and 24 μm bands.

Once the range of the brightness in some bands, mainly the lower limit of the brightness, is set up, the locations of the RSG stars can be delineated in the CMD with the help of the color index, and the AGB stars can be separated. Several near- and mid-infrared CMDs are shown in Figures 5 and 6, where the magenta solid line marks the upper limit of the luminosity, and the magenta dashed line marks the lower limit of the luminosity. The range of the color index is marked by red dashed–dotted line and blue dashed–dotted line. From multiple CMDs of M31 and M33, the following facts are observed:

1. The maximum luminosity of all sources agrees well with the theoretical limit of RSGs corresponding to $M = 27M_{\odot}$.
2. The minimum luminosity of all sources is about one magnitude above the theoretical limit of RSGs corresponding to $9M_{\odot}$. The reason may be the selection effect of observation that the fainter RSGs are not detected due to the sensitivity limit.
3. In the CMD of K_S versus $J - K_S$, the red limit is at $J - K_S = 1.60$, which is the limit of the carbon-rich and oxygen-rich stars from Hughes & Wood (1990). The blue limit is at $J - K_S = 0.50$, which is the observational limit of the RSGs in the Galactic halo obtained by Josselin et al. (2000).
4. In the [3.6] versus $J - [3.6]$ diagram, about 95% of the color index values lie within two standard deviations, and the limits of blue and red colors are set to include over 95% sources in the sample based on the distribution.
5. Because of the influence of the CO absorption line on the 4.5 μm band, the RSGs appear fainter in this band, so they look blue in the color index [3.6]–[4.5] and most of the sources have negative values.
6. In the CMDs of [8.0] versus $J - [8.0]$ and [8.0] versus $K_S - [8.0]$, $K_S - [8.0]$ becomes redder along with the increasing brightness in the [8.0] band due to the emission of circumstellar dust. A good linear relationship exists between the color index and the brightness at [8.0]. For M33, $[8.0] = -1.10 \times (J - [8.0]) + 16.26$ and $[8.0] = -1.09 \times (K_S - [8.0]) + 15.03$. For M31, $[8.0] = -1.20 \times (J - [8.0]) + 16.11$ and $[8.0] = -1.24 \times (K_S - [8.0]) + 14.80$. Therefore, the red limit of the color index is taken at the intersection point of the fitting line and the upper limit of the luminosity. Once the red limit is set, the blue limit is set to ensure the probability that lies in the range between the limits of blue and red colors is 95% based on the distribution.
7. In the CMD of [24] versus [8.0]–[24], due to the influence of the infrared emission of circumstellar dust on the 24 μm band, some sources supersede the theoretical luminosity upper limit of the RSGs. The limits of the color index [8.0]–[24] are set to include over 95% stars in the sample based on the distribution.

In order to clear of the pollution of AGB stars, sources that are fainter than the lower limit of K_S, [3.6], [8.0], and [24] bands are removed.

Sources that are bluer than the blue limit of $J - K_S$ or the blue limit of $J - [3.6]$ should be removed as well. As for color indexes of $J - [8.0]$, $K_S - [8.0]$, and $[8.0] - [24]$, they are not reasonable criterion due to the impact of circumstellar dust, and we only mark the range of these three color indexes by experience.

In the CMDs of M33, 36 sources are bluer than the blue limit of $J - K_S$ or $J - [3.6]$; however, 16 of them have been identified as RSGs by spectroscopy (Massey & Evans 2016). In addition, 1, 1, 2, and 6 sources are fainter than the lower limit of the *Spitzer*/IRAC [3.6], [5.8], [8.0], and *Spitzer*/MIPS [24] band, respectively. In total, 30 sources are removed finally.

For M31, 22 sources are bluer than the blue limit of $J - K_S$ or $J - [3.6]$; however, 11 of them have been identified as K-type or M-type supergiant stars by spectroscopy (Massey & Evans 2016) so they are kept, and 1 of these sources is also fainter than the lower limit of the *Spitzer*/IRAC [3.6] band magnitude. Besides, 1 source is fainter than the lower limit of the *Spitzer*/MIPS [24] band magnitude and is removed. In total, 12 sources are removed.

We are left with the samples of 717 RSGs in M33 and 420 RSGs in M31 at last.

3. Time-domain Data

3.1. The iPTF Data

The time-series data is taken from the iPTF survey, a wide-field survey for an exploration of optical transients using the 1.2 m Samuel Oschin Telescope at Palomar Observatory (Law et al. 2009; Rau et al. 2009). This survey uses a large field camera covering 7.8 square degrees with 11 2048 × 4096 charge-coupled devices (CCDs) at a resolution of 1.01 arcsec/pixel. In the iPTF survey, 2 and 6 frames covered the M33 and M31 sky area, respectively, from 2009 August to 2015 January (about 2000 days in total) with a typical seeing of 2 arcsec. Although the images were taken in both R and g bands, the R-band observations are dominant and make use of >80% time, reaching 20.5 mag at a 5σ level. Therefore, we choose the R-band iPTF data to analyze the variation of RSGs. The RSGs are selected in the iPTF images within three arcseconds from the position of the star. Figures 7 and 8 show the iPTF images that include 658 and 377 RSG stars in M33 and M31, respectively, whose light variations are further analyzed.

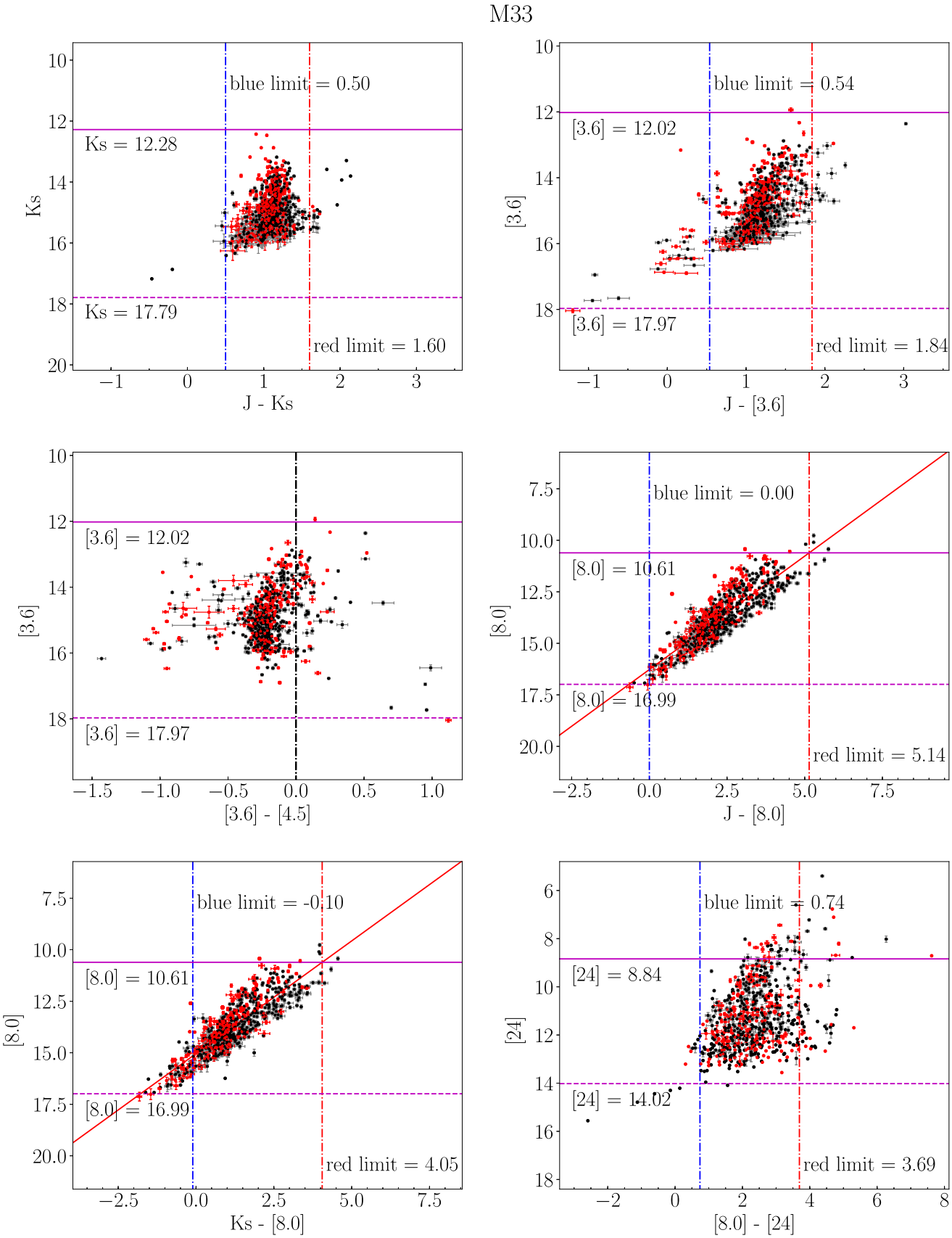

Figure 5. CMDs for RSG candidates in M33. The magenta solid line indicates upper limit of the magnitude in each band, the magenta dash line indicates lower limit of the magnitude in each band, the red dashed–dotted line indicates the red limit of RSGs, and the blue dashed–dotted line indicates the blue limit of RSGs. Red dots are sources confirmed by the spectrum.

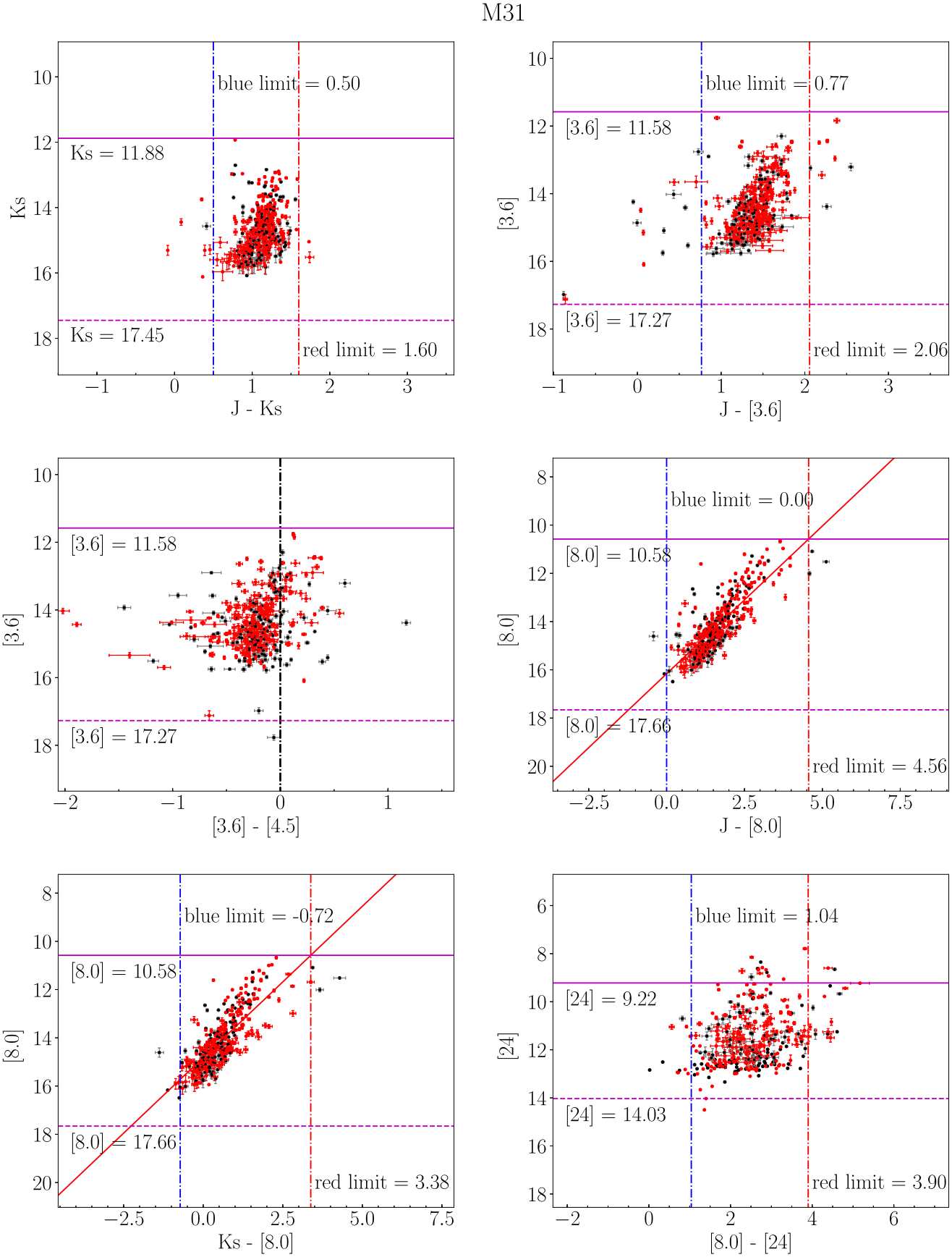

Figure 6. CMDs for RSG candidates in M31. The symbol convention is the same as in Figure 5.

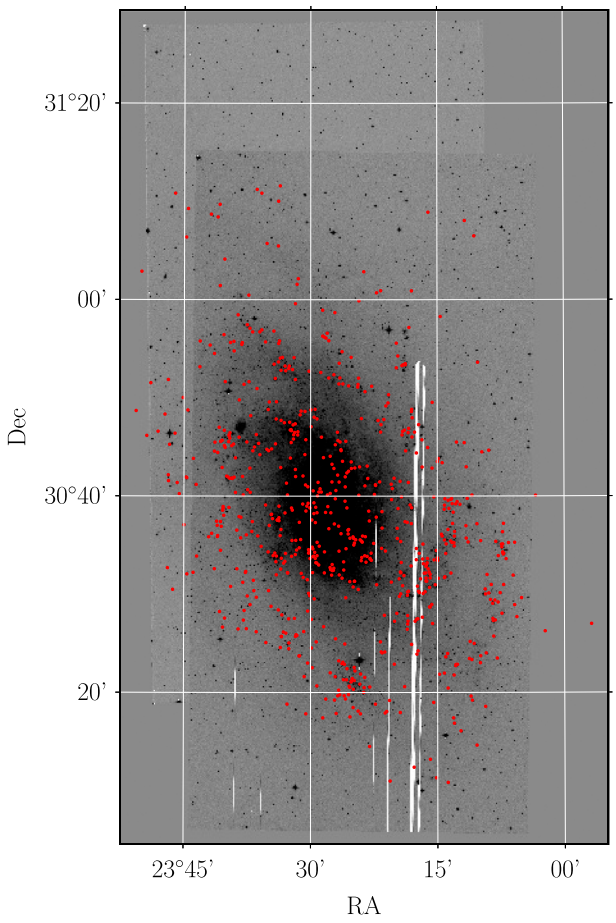

Figure 7. iPTF image of M33 with the red dots for the position of RSGs.

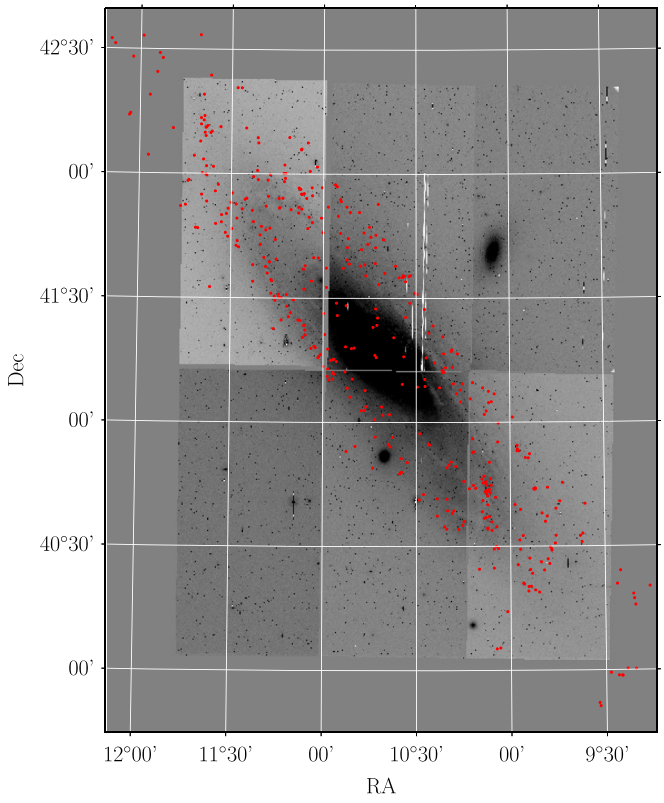

Figure 8. iPTF image of M31 with the red dots for the position of RSGs.

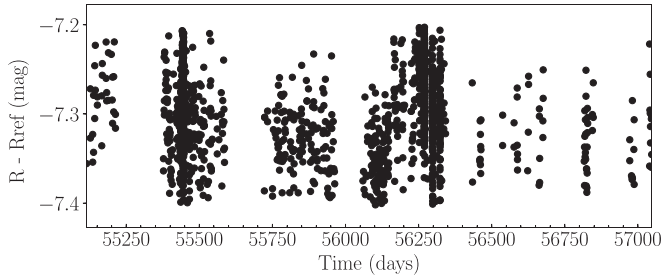

Figure 9. Performance of the artificial reference star. *Rref* represents the *R* -band magnitude of the artificial reference star, and *R* represents the *R*-band magnitude of the selected Tycho reference star.

3.2. Photometry

The CCD images were processed in a standard way. We measured all the iPTF images available (796 images of M33 and 1980 images of M31) using the SExtractor code (Bertin & Arnouts 1996) with fixed coordinates. For a precise photometry, a stable reference star should be chosen for differential photometry, and its brightness and color should be similar to the target stars in order to cancel the influence of the instruments and atmosphere as much as possible. For this purpose, we made an artificial reference star whose brightness is the average of all the red supergiant stars in each image, i.e., the average of approximately 700 RSGs in M33 and 100 RSGs in M31 within one image. Naturally, this artificial star has the very typical color of RSGs. The large scale of the sample should smooth out the variation of all RSG stars, which makes the artificial reference star stable. The stability of the brightness is checked by comparing with a star from the Tycho reference catalog (Hog et al. 1998) with a brightness of $VT = 12.608$ mag and a color of $VT - BT = 1.704$, which is similar to RSGs. As shown in Figure 9, the standard error of differential photometry between the artificial reference star and the Tycho reference star is about 0.04 mag, which implies that the photometric accuracy is better than 0.04 mag. Considering this Tycho reference star is much brighter than the RSGs, the real accuracy should be even better. In order to achieve a good photometry quality, the size of the aperture is adjusted according to the FWHM of the point-spread function (PSF) in each image by $R_{\rm aperture} = 1.5 + 1.2 \times {\rm FWHM}$.

4. Period Determination

Before we start to determine the period of light variation, the original photometric data from differential photometry are processed further. First, the outlying points are removed using the locally weighted linear regression, with its most common method known as locally estimated scatterplot smoothing (LOESS). The weight function used for LOESS is the Gaussian function: $\omega(x, z) = \exp(-(x - z)^2/2\kappa^2)$, where we adopted $\kappa = 4.5$ with eye-check after trying the value in the range of [0.01,10]. The points lying more than 3σ away from the locally fitting line are removed. Then, the moving-average filter was used to smooth the light curve, in which a window of nine days is taken. Figure 10 illustrates an example showing the two processes and the resulting light curve for period determination.

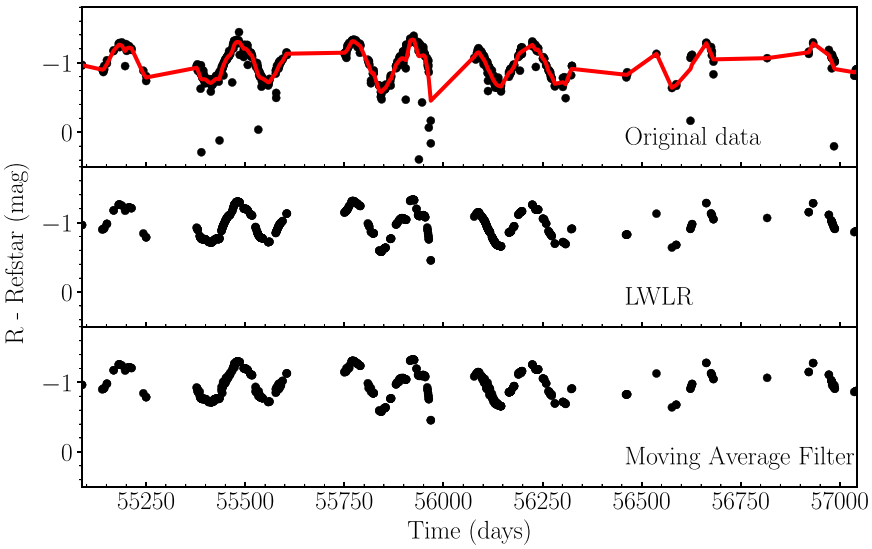

Figure 10. Data preprocessing. The top panel shows the original data, and the red line shows the fitting curve using locally weighted linear regression. The middle panel shows the data after removing the points that lie more than 3σ away from the light curve. The bottom panel shows the data that is smoothed by moving-average filter.

Table 3
The Parameters Used for the Period Determination

Input Parameters	GLS	DFT	WWZ	PDM
Minimum period	10	10	10	10
Maximum period	3500	3500	⋯	3500
Period step	0.01	0.01	⋯	0.50
Time-shift step	⋯	⋯	20	⋯
Frequency sampling	⋯	⋯	0.5714	⋯
Software	VARTOOLS	VARTOOLS	VARTOOLS	PyAstronomy

For the period determination of nonuniformly sampled data as the present case, no single algorithm is fully suitable. It is necessary to use various methods to cross-check the existence of periodicity. The popular methods for the determining period are the Phase Dispersion Minimization (PDM; Stellingwerf 1978) algorithm based on the time domain, the Generalized Lomb–Scargle periodogram (GLS; Zechmeister & Kurster 2009) algorithm based on the frequency domain, the Weighted Wavelet Z-transform (WWZ; Foster 1996) algorithm based on the time-frequency, and the discrete Fourier transform (DFT) based on frequency domain. All these four methods are applied to the light curves of the RSGs in M33 and M31.

The PDM method looks for the period that brings about the minimum phase dispersion designated by Θ in a number of trial periods. The GLS method is an improvement on the traditional Lomb–Scargle (LS; Lomb 1976; Scargle 1982) method. The main improvement is that the GLS algorithm uses the sine function of the addition constant C to fit the time-series data and each calculation takes into account the effect of observation error ω. Therefore, the period estimation accuracy of the GLS algorithm is better than that of the LS algorithm. The WWZ method is a period determination algorithm based on wavelet analysis and vector projection that are very suitable for the analysis of nonstationary signals and has advantages in the analysis of time-frequency local characteristics. The DFT method is a classical period determination algorithm based on Fourier transform.

We use the GLS, DFT, and WWZ methods from the astronomical time series analysis program (VARTOOLS; Hartman & Bakos 2016) and PDM (Stellingwerf 1978) method from PyAstronomy for the period determination. The parameters used in the methods are shown in Table 3 in detail. The final selection of the period depends on the goodness of fitting the light curve. A period is assigned to an object with semi-regular variation only when it is detected by at least two methods whose difference in period is usually (>70%) less than 40 days while up to 50–90 days in a few cases. The period is searched continuously in the power spectrum of the residual data after subtracting the light variation with the most prominent period until the local signal-to-noise ratio of the power spectrum is less than 4. Figure 11 shows an example of period determination, where both the PDM and GLS methods find a period at ∼347 days, and the WWZ method also confirms that this period is present in most of the observational time. Based on the period and the regularity of light variation, these RSGs are classified into five categories:

1. Semi-regular variables, marked as ***S***, which definitely have a period and are used for the follow-up analysis of the P–L relations. There are 84 (56) sources in M33 (M31).
2. LSP variables, marked as ***L***, which show evidence of LSP while the LSP cannot be determined accurately due to the limited time span of the iPTF data (∼2000 days). There are 48 (13) sources in M33 (M31).

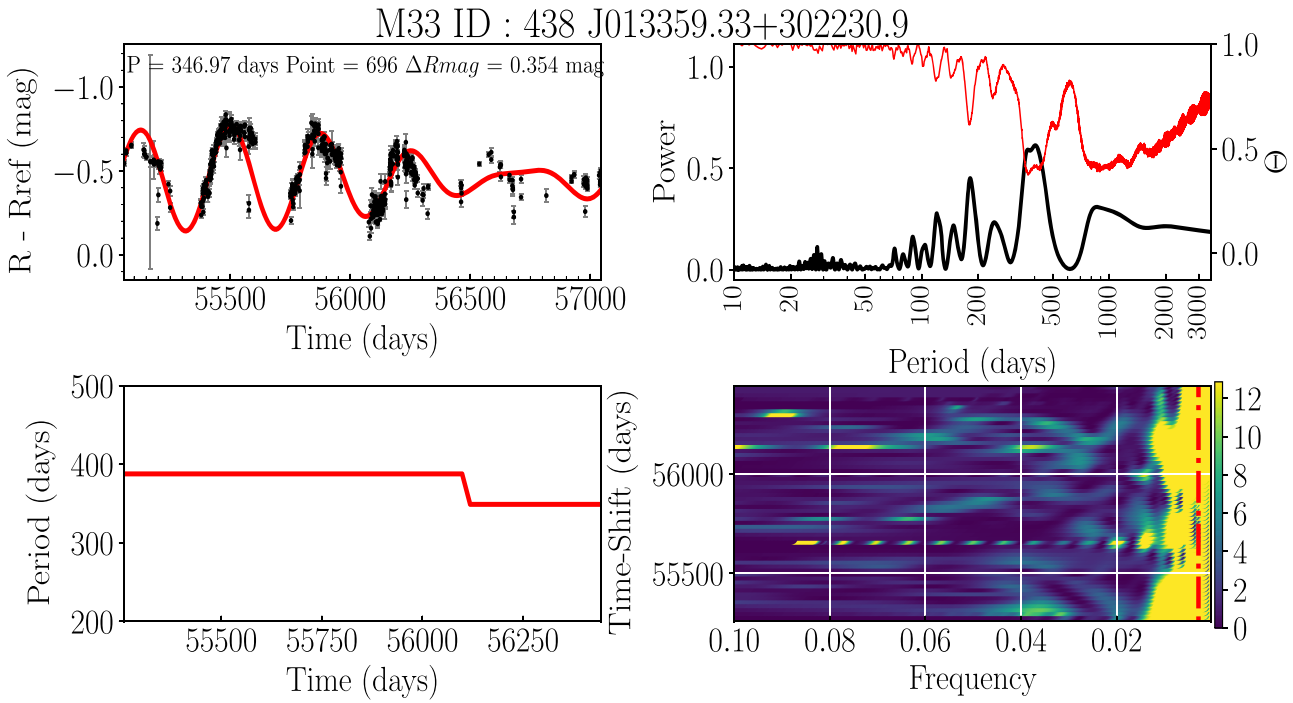

Figure 11. Example of the period determination from the light curve of an RSG with semi-regular variation. The left top panel is the light curve (black dots with an error bar) and the fitting result (red line). The results of the PDM (Θ—P, red line) and GLS (Power—P, black line) analysis are shown in the top right panel. The result from WWZ is shown in the bottom panels, where the right shows the WWZ map and the left shows the period against time.

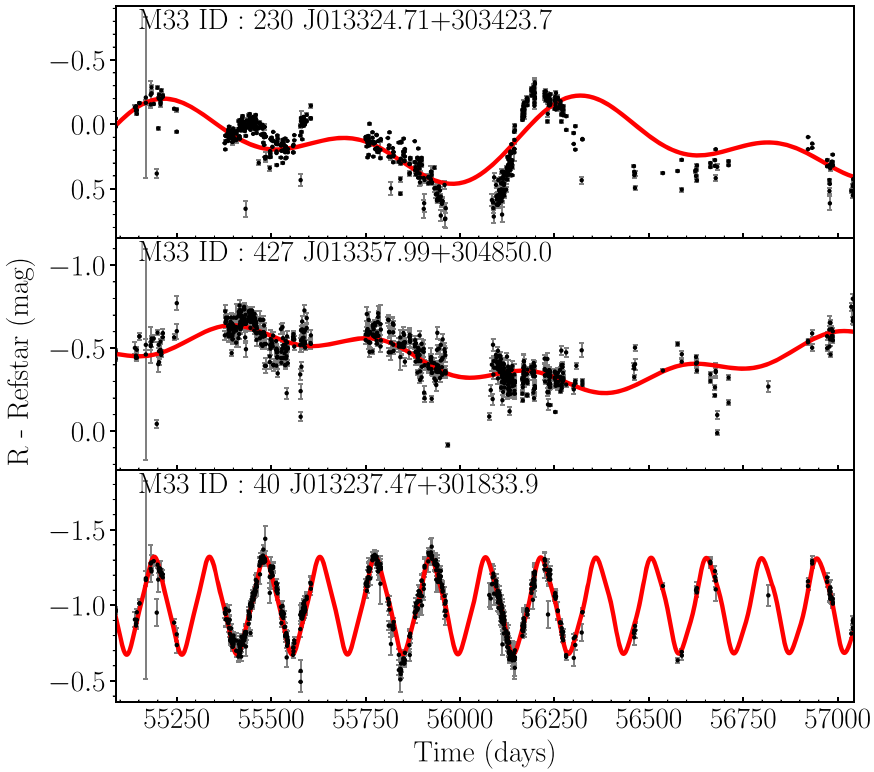

Figure 12. Three categories of light curve. From top to bottom are the irregular, long secondary period, and semi-regular variables.

3. Irregular variables, marked as ***I***, which have small amplitudes and too complex variation to show any periodicity. There are 14 (21) sources in M33 (M31).
4. Undefined classes, marked as ***U***, which lack enough observational data to determine its variability. There are 86 (18) sources in M33 (M31).
5. No significant variables, marked as ***N***, which have no significant variation. There are 426 (269) sources in M33 (M31).

The light curves of the examples of the first three types are shown in Figure 12.

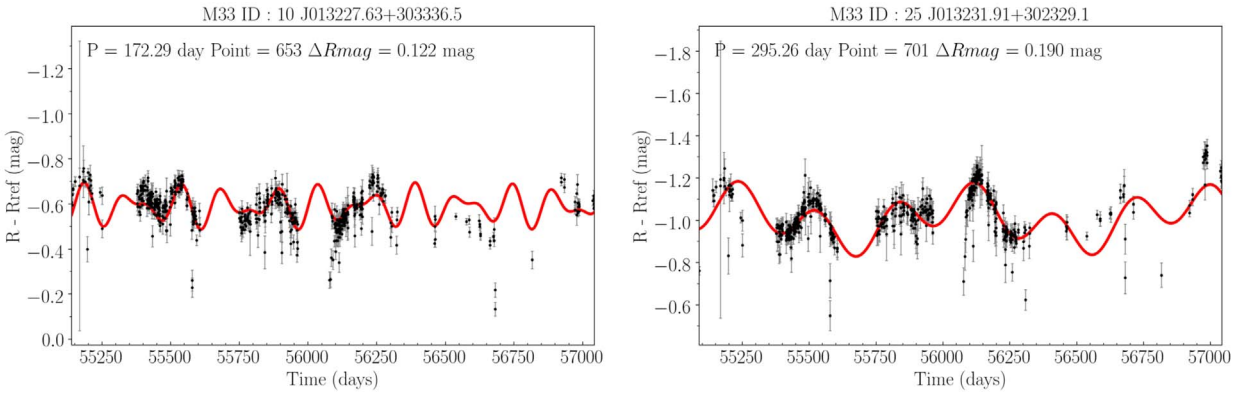

Figure 13. Light curve of RSGs with Semi-Regular Variation in M33. (An extended version of this figure is available.)

The light curves with the fitting of all stars are displayed in Figures 13 and 14, and the properties of variation and photometric results are included in Tables 4 and 5.

In addition, three stars exhibit very regular light variation, which are J004115.35+405025.2 and J004415.42+413409.5 in M31 and J013237.47+301833.9 in M33. Among them, J004115.35+405025.2 and J004415.42+413409.5 are also studied by Soraisam et al. (2018). These sources have relatively short period (96.5, 76.5, and 146.5 days, respectively). The spectral types are identified as K1 for J004115.35+405025.2, K2 for J004415.42+413409.5, and RSG for J004415.42 +413409.5 (Massey & Evans 2016). As discussed previously, the luminosity of these stars indicates that they are supergiants, which means that some RSGs may have regular variation. The next section will show that these stars very possibly pulsate in the first overtone mode. These three RSGs are plotted in the H–R diagram in Figure 15. It can be seen that RSG J013237.47 +301833.9 in M33 lies in the instability strip (IS), while J004115.35+405025.2 and J004415.42+413409.5 in M31 are very close to the IS. Moreover, these stars are at the faint end of the RSGs, which implies relatively low masses. We may say that these regular variables are RSGs with relatively low masses and relatively high temperatures. On the other hand, there are some other sources also in the IS, and they are not regular variables but are semi-regular variables. The YSG is known to be a kind of Cepheid; meanwhile, RSGs and YSGs as are hard to distinguish near the blue limit of RSGs as the three regular variables are. It can be concluded that Some RSGs with early K spectral types may lie in the IS and have very regular variations.

5. P–L Relation

The P–L relation is derived for the bands with photometric data available, from the optical V band through 2MASS near-infrared JHK_S bands to the *Spitzer*/IRAC and *Spitzer*/MIPS bands. As mentioned earlier, we only adopted the RSGs that show semi-regular variation and whose periods are found by at least two methods.

The observational results are compared with the model by Guo & Li (2002) in Figures 16 and 17. The absolute magnitude in the K_S band of the model is obtained from the absolute bolometric luminosity with the help of the bolometric correction in the K_S band by Josselin et al. (2000). Although the models are not perfectly matched with the observation, two sequences are clear in that most of the stars follow the sequence of the fundamental-mode pulsation and a few stars are closer to the first overtone pulsation mode. The three regular variables are all located close to the first overtone model. Because the pulsations of the fundamental and first overtone modes follow different P–L relations, they must be separated to study this relation. We identify 19 stars in M33 and 7 stars in M31 pulsating in the first overtone mode, and their P–L relation is not analyzed due to too few stars. Nevertheless, there is no clear indication of a P–L relation for them. The P–L relation of the 65 RSGs in M33 and 49 RSGs in M31 that pulsate in the fundamental mode is then analyzed.

In principle, the brightness should be the mean magnitude when the P–L relation is dealt with. However, the brightness in the V band is taken from the single measurement by LGGS. Since the amplitude of variation in the V band is $\sim$1 mag, this can cause some dispersion in the P–L relation in the V band. Although the brightness in the infrared bands is also taken from the single measurement, the small amplitude of variation makes the single measurement approximate to the mean brightness and does not bring significant scatter in the P–L relation.

Following the convention, a linear function is taken to fit the relation between the absolute magnitude and log P. The results are displayed in Figures 18 and 19 and Table 6 for the M33 sample, and in Figures 20 and 21 and Table 7 for the M31 sample. It is apparent that there is a tight relation in the near-infrared and the mid-infrared band. Quantitatively, the correlation coefficients are around 0.8 (see Tables 6 and 5), although it becomes less tight at the *Spitzer* [8.0] and [24] bands, which is due to the scattering brought by circumstellar dust. On the other hand, the V band shows almost no relation between the brightness and period. The lack of P–L relation in the V band may be caused by the large, inhomogeneous interstellar extinction, which is about 10 times that in the K_S band (Cardelli et al. 1989; Wang & Jiang 2014) in addition to the relatively large amplitude of variation. With no accurate measurement of interstellar extinction to an individual star, we applied the Wesenheit index, $W_{BV} = V - R_V(B - V)$. The parameter R_V ($\equiv A_V/E(B - V)$, the total-to-selective extinction ratio) has an average value of 3.1 in the Milky Way, while it is not well determined in M31 and M33. This value is found to vary from about 2.0 to 3.3 toward different sightlines in M31 (Dong et al. 2014; Clayton et al. 2015), and it is not well measured in M33. We take the value of 3.1 for simple and reasonably good approximation. Figures 19 and 21 illustrate the relation of W_{BV} with log P. The relation is much improved in that the correlation coefficient is increased to around 0.4 (see the last

Table 4
Parameters of RSGs in M33

ID	LGGS	...	*J*	*H*	*Ks*	GLS	DFT	PDM	WWZ	Period	GLS-2	DFT-2	PDM-2	WWZ-2	Period-2	Amplitude	Type	Rms
1	J013147.31 +302659.0	...	16.72	15.982	15.786	…	…	…	…	…	…	…	…	…	…	…	…	…
2	J013209.23 +302614.8	...	16.671	15.812	15.293	…	…	…	…	…	…	…	…	…	…	…	…	…
3	J013213.60 +304003.4	...	16.76	16.162	15.1	386.808	77.799	187.5	91.842	77.799	33.802	232.955	187.5	317.273	317.273	0.117	U	0.1421
4	J013220.36 +302938.0	...	…	…	…	881.409	793.248	1782.5	875	793.248	12.901	134.165	386	125	134.165	0.023	N	0.0715
5	J013222.59 +302741.8	...	16.669	15.746	15.77	34.058	15.841	2099	3500	15.841	3461.532	31.483	2099	1166.667	31.483	0.017	N	0.0743

(This table is available in its entirety in machine-readable form.)

Table 5
Parameters of RSGs in M31

ID	LGGS	...	*J*	*H*	*Ks*	GLS	DFT	PDM	WWZ	Period	GLS-2	DFT-2	PDM-2	WWZ-2	Period-2	Amplitude	Type	Rms
1	J003703.64+402014.9	...	16.583	15.704	15.72	…	…	…	…	…	…	…	…	…	…	…	…	…
2	J003721.98+401543.3	...	…	…	…	…	…	…	…	…	…	…	…	…	…	…	…	…
3	J003722.34+400012.1	...	16.045	15.368	15.026	…	…	…	…	…	…	…	…	…	…	…	…	…
4	J003723.56+401715.5	...	15.697	14.872	14.833	…	…	…	…	…	…	…	…	…	…	…	…	…
5	J003724.48+401823.3	...	16.236	15.006	15.11	…	…	…	…	…	…	…	…	…	…	…	…	…

(This table is available in its entirety in machine-readable form.)

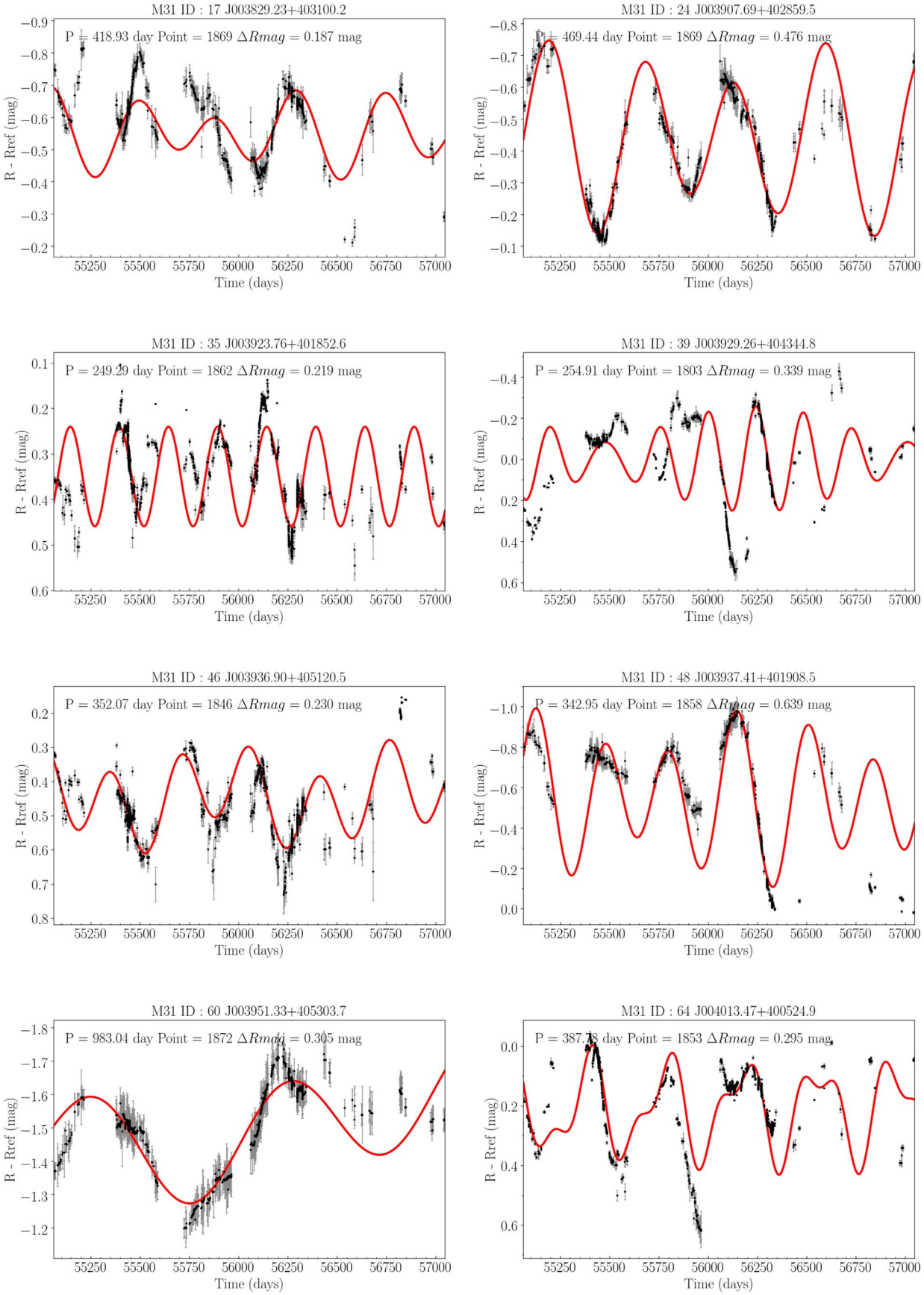

Figure 14. Light curve of RSGs with semi-regular variation in M31. (An extended version of this figure is available.)

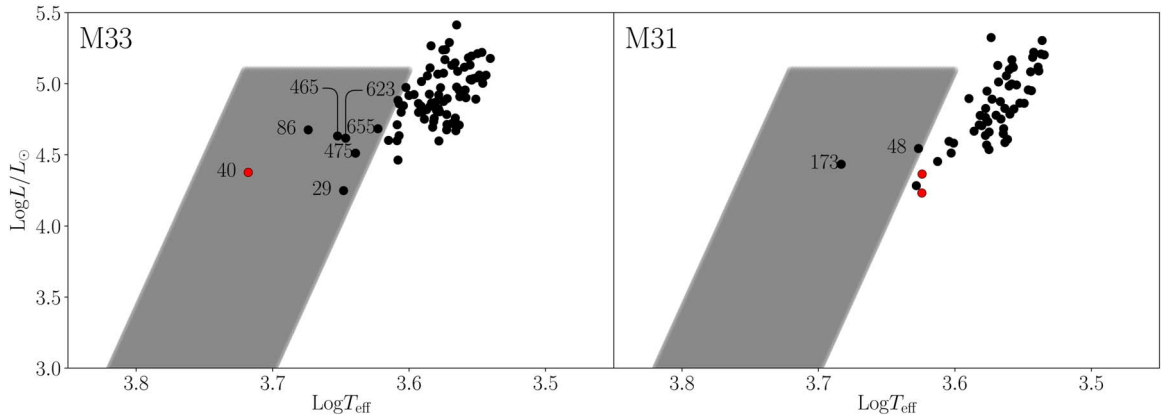

Figure 15. H–R diagram for RSGs with semi-regular variation in M33 (left) and M31 (right). The gray shaded area represents the IS (Tammann et al. 2003). Red dots are the regular variables, and black dots with ID from Tables 6 and 5 are the RSGs in the IS.

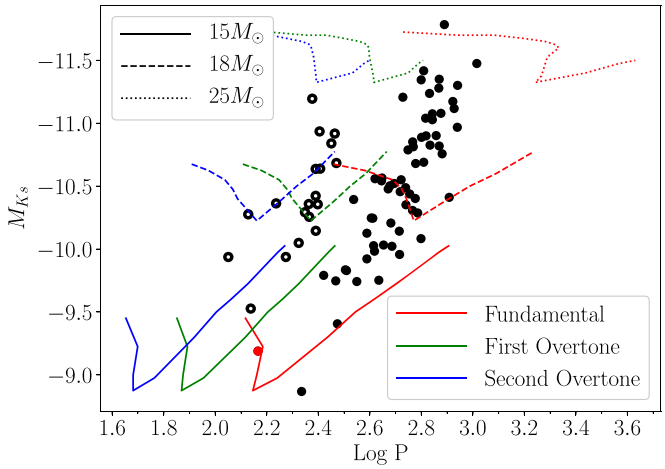

Figure 16. Locations of the RSGs in M33 in the absolute K_S magnitude vs. log P diagram. The lines are based on the model calculations by Guo & Li (2002) at metallicity $Z = 0.02$. The solid black dots are identified as pulsating in the fundamental pulsation mode, the black circles in the first overtone pulsation mode, and the red dot is the RSG with regular variation.

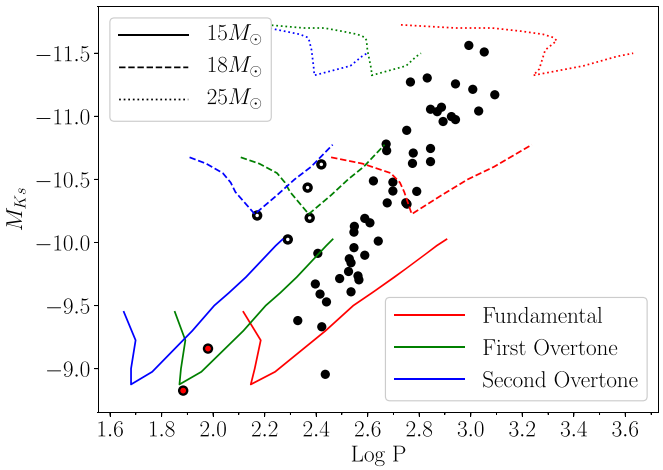

Figure 17. Same as in Figure 16, but for M31.

row of Tables 6 and 7), which verifies that the lack of P–L relation in the V band is partly caused by interstellar extinction. For a correct P–L relation in the V band, an accurate correction of interstellar extinction should be made to each star individually and accurately. In summary, the P–L relation exists between the photosphere brightness and the period of light variation for RSGs with semi-regular variation in M33 and M31. There is a tight P–L relation for apparent brightness in the 2MASS/JHK_S and *Spitzer*/IRAC1-3 bands. Meanwhile, the P–L relation should exist and can show up in the V band when the interstellar extinction is corrected, and it will become tighter in the *Spitzer* [8.0] and [24] band when the emission of circumstellar dust is subtracted.

Table 6
The Parameters of the P–L Relations of RSGs in M33

Band	Slope	Intercept	Correlation
M_V	−0.23	−4.99	−0.07
M_J	−2.69	−2.08	−0.79
M_H	−3.02	−1.99	−0.84
M_{K_S}	−3.18	−1.87	−0.85
$M_{[3.6]}$	−3.84	−0.24	−0.85
$M_{[4.5]}$	−4.15	0.73	−0.82
$M_{[5.8]}$	−4.57	1.42	−0.82
$M_{[8.0]}$	−5.01	1.74	−0.75
$M_{[24]}$	−6.32	3.31	−0.73
W_{BV}	−2.01	−6.40	−0.46

Note. This table shows the parameters slope, intercept, and correlation from P–L relation of RSGs in M33.

6. Comparison with Other Results

For further comparison with other results, we chose the K_S band as a luminosity indicator and run Markov chain Monte Carlo (MCMC) using PyMC3 (Salvatier et al. 2016) to obtain the uncertainty of the relation after taking the photometric error into account. The P–L relation in K_S band is as follows:

For M33, $M_{K_S} = (-3.18 \pm 0.46) \times \log P + (-1.87 \pm 0.31)$.

For M31, $M_{K_S} = (-3.01 \pm 0.38) \times \log P + (-2.29 \pm 0.24)$.

6.1. M33

Yang & Jiang (2012) derived the P–L relation of 40 RSGs in M33 from a sample by Kinman et al. (1987): $M_K = (-3.59 \pm 0.41) \times \log P + (-0.88 \pm 0.69)$. The P–L

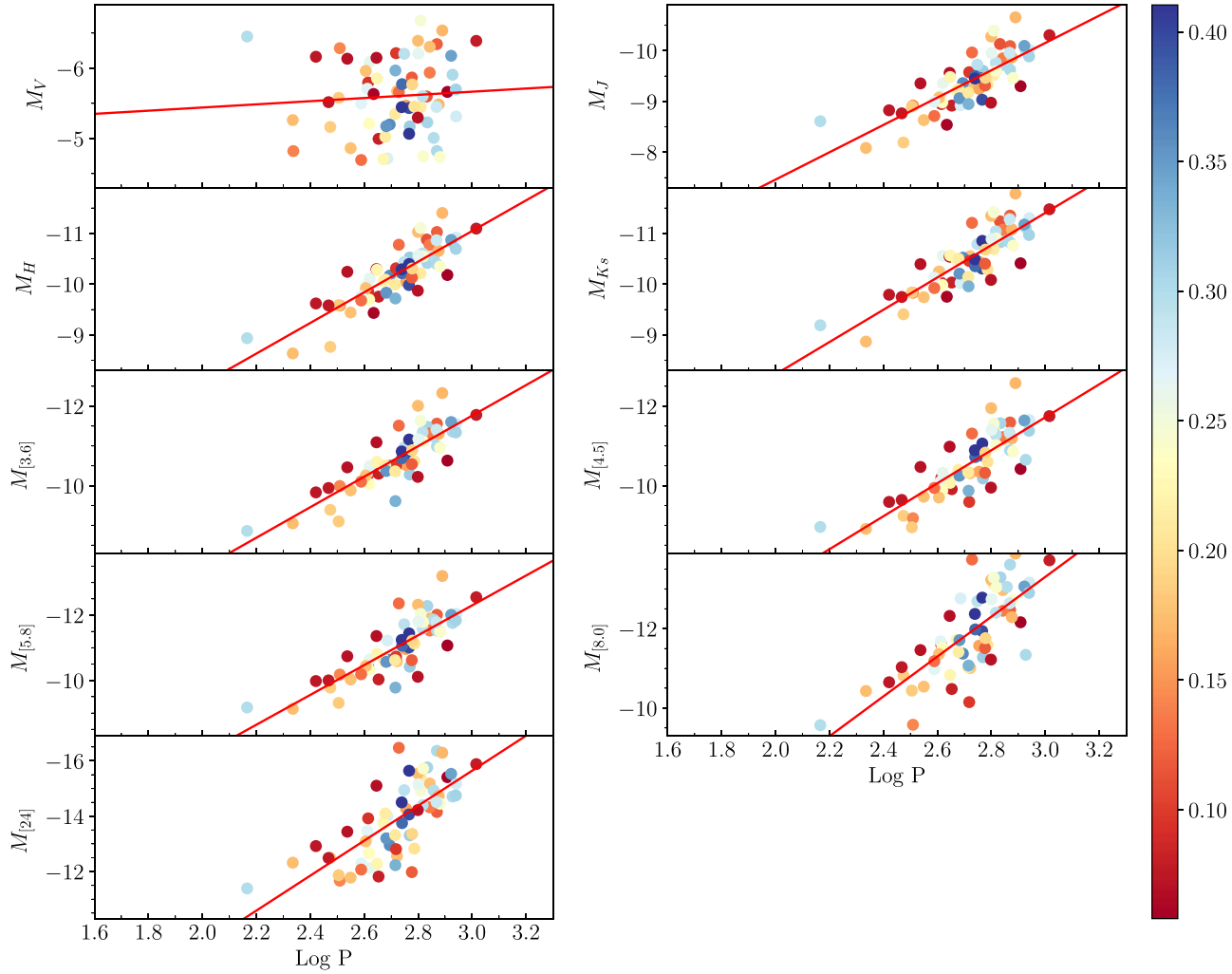

Figure 18. P–L relation in the V, J, H, K_S, *Spitzer*/IRAC [3.6], [4.5], [5.8], [8.0], and MIPS [24] bands for RSGs with semi-regular variation in M33. The red solid line is a linear fit between the multiband absolute magnitude and the period. The color of dots decodes the variation amplitude in accord with the color bar (in the unit of magnitude).

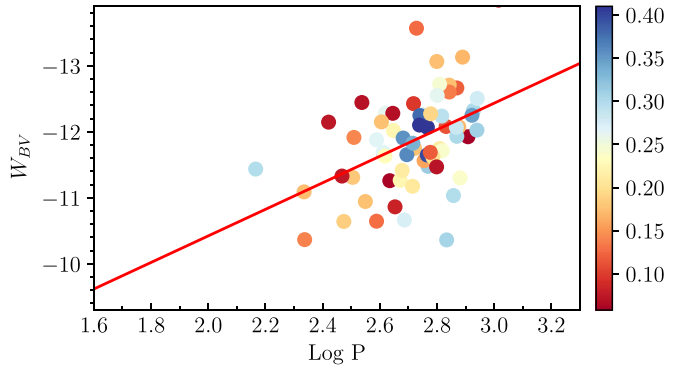

Figure 19. P–L relation in the W_{BV} band for RSGs with semi-regular variation in M33. The symbols are the same as in Figure 18.

relation is in agreement with this work within a reasonable error range as shown in Figure 22. However, we derived the P–L relation based on a larger sample of 84 sources with semi-regular variation and a longer time baseline. Moreover, the P–L relation is derived in many more bands, including the visual V band, other 2MASS bands, and the *Spitzer* bands.

6.2. M31

The P–L relation of RSGs in M31 was obtained previously in the K band by Soraisam et al. (2018) who also used the iPTF data. Their data spanned from MJD 56,000 to 58,000. Here, we used the iPTF data from MJD 55,050 to 57,050 by the limit to data access. Soraisam et al. (2018) compared with the theoretical P–L relation from Modules for Experiments in Stellar Astrophysics (Paxton et al. 2011, 2013, 2015, 2018). Consistent with our results, the majority of sources pulsate in the fundamental mode. After ignoring 10 RSGs in the first overtone pulsation mode and 2 RSGs with periods <100 days, they obtained the P–L relation: $M_K = (-3.38 \pm 0.27) \times \log P + (-1.32 \pm 0.75)$. This P–L relation is also in agreement with our work within the error range, as shown in Figure 22.

6.3. The Galaxy, the LMC, and the SMC

Kiss et al. (2006) derived P–L relation based on 18 RSGs in the Milky Way and the light curves collected by AAVSO. Most of these RSGs are members of associations and clusters, and their distances are taken as those of the host associations and clusters. For three sources, they used the *Hipparcos* parallaxes.

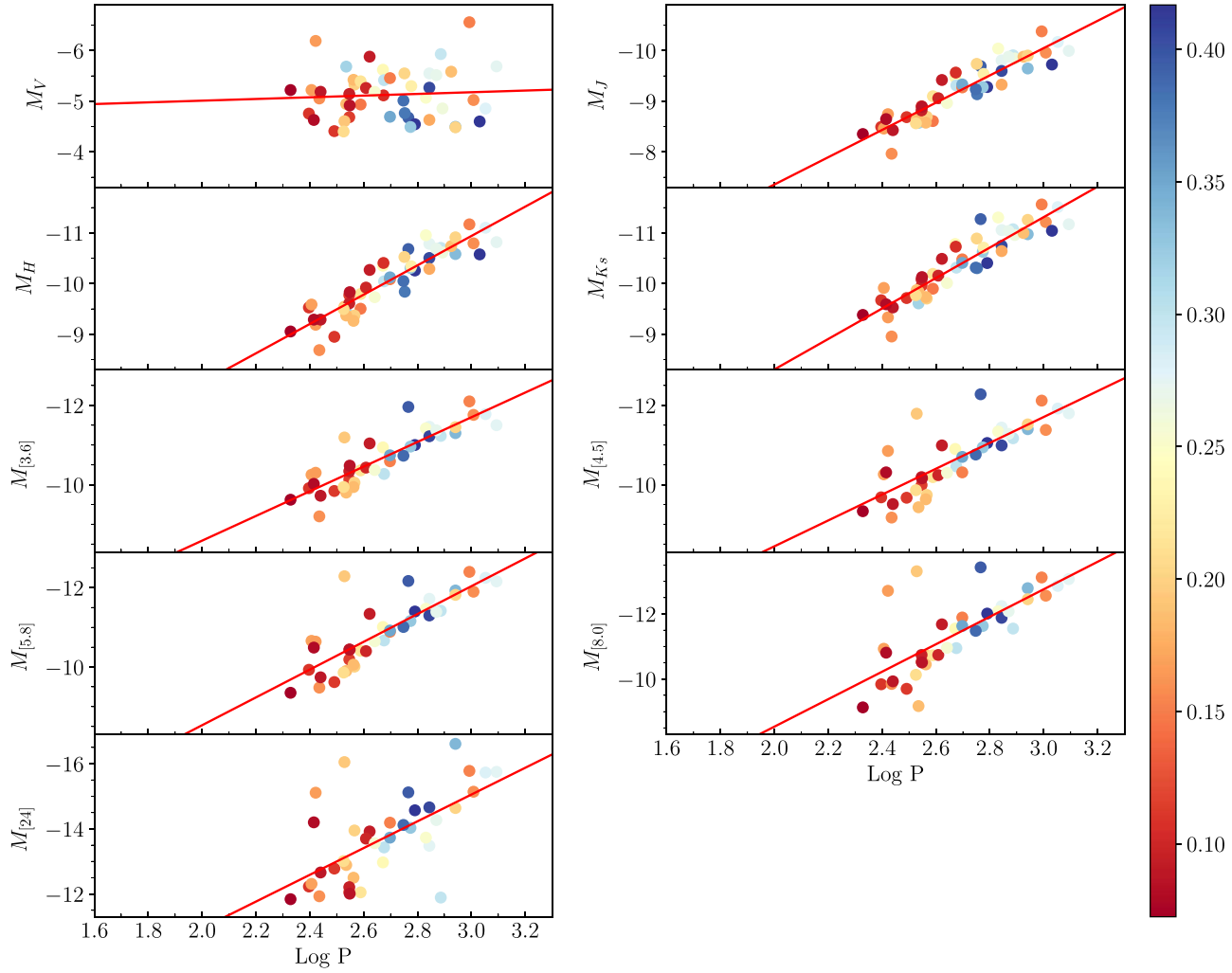

Figure 20. Same as in Figure 18, but for M31.

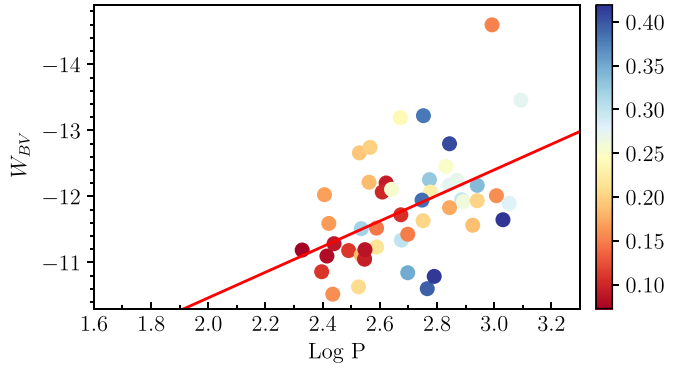

Figure 21. Same as in Figure 19, but for M31.

Table 7
The Parameters of the P–L Relations of RSGs in M31

Band	Slope	Intercept	Correlation
M_V	−0.17	−4.68	−0.07
M_J	−2.69	−1.97	−0.92
M_H	−2.90	−2.25	−0.91
M_{Ks}	−3.01	−2.29	−0.92
$M_{[3.6]}$	−3.11	−2.36	−0.87
$M_{[4.5]}$	−3.26	−1.92	−0.80
$M_{[5.8]}$	−3.51	−1.52	−0.83
$M_{[8.0]}$	−4.22	−0.10	−0.74
$M_{[24]}$	−4.11	−2.73	−0.63
W_{BV}	−1.94	−6.59	−0.48

Note. This table shows the parameters slope, intercept, and correlation from P–L relation of RSGs in M31.

Based mainly on the ASAS and MACHO data, Yang & Jiang (2011, 2012) derived the P–L relation of 47 RSGs in the LMC and 21 RSGs in the SMC. Comparison of the P–L relations of RSGs in different galaxies are shown in Figure 23. It can be seen that the P–L relation in M33 is very similar to the SMC. The P–L relations seem to be similar in these galaxies except for the Milky Way. The P–L relation of RSGs in the Milky Way appears a little different, which may be caused by the dispersion of the estimated distance and interstellar extinction. It may be argued that the P–L relations in *K* band is universal in these nearby galaxies. It should be mentioned that the optical bands would be better to examine the dependence of the P–L relation on metallicity because the P–L relation is less dependent on metallicity in near-infrared bands than in optical bands (Bhardwaj et al. 2017). Nevertheless, interstellar extinction is serious to make the determination of P–L relation more uncertain in optical bands.

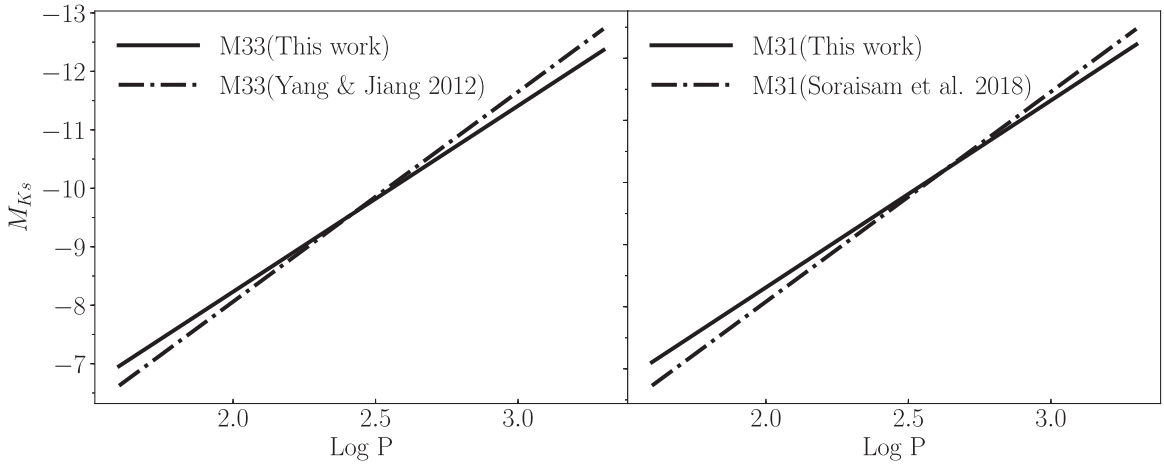

Figure 22. Comparison of the P–L relations of RSGs in M33 and M31 with previous works.

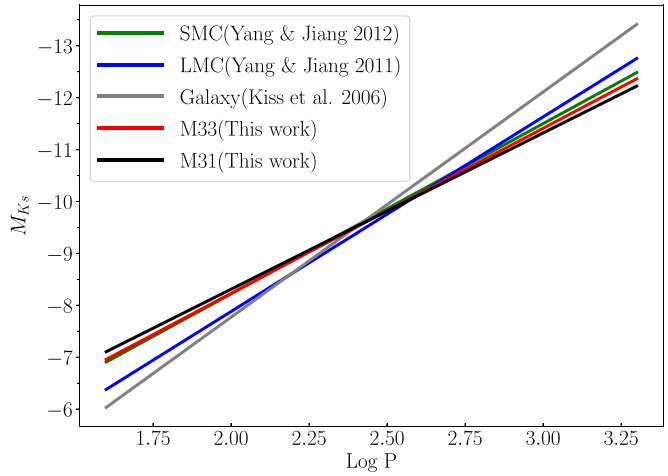

Figure 23. P–L relations of RSGs in nearby galaxies and the Milky Way.

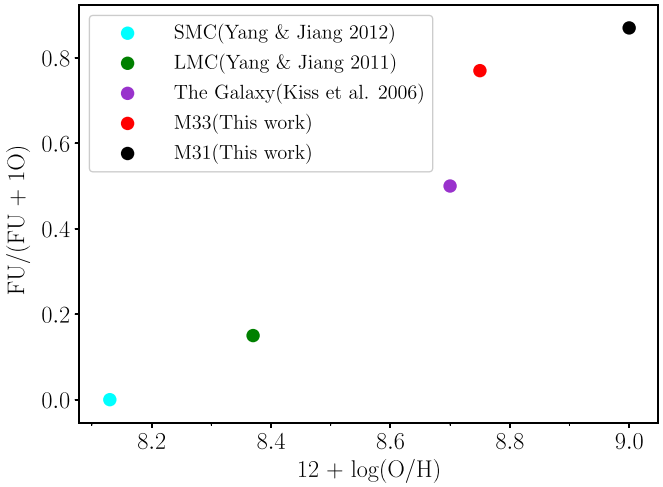

Figure 24. Number ratio of FU/(FU + 1O) vs. metallicity in nearby galaxies and the Milky Way.

The ratio of $N_{\rm FU}$ (the number of RSGs that pulsate in FU pulsation mode) to $N_{\rm 1O}$ (the number of RSGs that pulsate in 1O pulsation mode) increase with the metallicity. The values $N_{\rm FU}/(N_{\rm FU}+N_{\rm 1O})$ vary from the SMC (0%), the LMC (15%), the Galaxy (50%), and M33 (77%) to M31 (87%), as shown in Figure 24 when we compare the results of the SMC, LMC, and Galaxy from Yang & Jiang (2012). The percentages may suffer some uncertainty because the identification of pulsating mode depends on the theoretical models adopted and the borderline between the two modes is not very sharp. However, it is apparent that $N_{\rm FU}/(N_{\rm FU}+N_{\rm 1O})$ increases with metallicity. We explored the underlying physics and found that this may be related to convection. Yecko et al. (1998) calculated the turbulent convective Cepheid models and found that the 1O mode would be suppressed at a large mixing length in comparison with the FU mode, which may be understood because the 1O mode occurs in a relatively shallower layer and would be influenced more by the envelope convection. Although this model is for Cepheids, it should be applicable to RSGs since RSGs have even stronger convection due to lower effective temperature. Furthermore, Chun et al. (2018) found that the mixing length increases with the metallicity for RSGs. This may be caused by that high metallicity leads to less effective radiative transfer due to higher opacity, and consequently, stronger convection is needed. Combining the two theories—the 1O mode would be suppressed at large mixing length and the mixing length increases with metallicity —we can expect that the 1O mode pulsation occurs less frequently at high metallicities. Specifically, the 1O mode pulsators should be the least frequent and thus the largest FU/(FU + 1O) occurs in M31 with the highest metallicity.

7. Summary and Conclusion

The study is based on a relatively complete and pure sample of RSGs in M33 and M31. From the preliminary samples of RSGs (749 in M33 and 437 in M31), which were selected by the visual colors with the LGGS multiband photometry, the foreground dwarf, and giant stars (two in M33 and five in M31) are further excluded according to their distance modulus from the *Gaia* DR2 catalog. The pollution of AGB stars in the local galaxy is carefully checked by the locations in several CMDs, which found almost no contamination by AGB stars while the dust emission has the significant influence on the flux in the mid-infrared bands, such as the *Spitzer*/[8.0] and [24] bands. Consequently, we find that there are 717 RSGs in M33 and

420 RSGs in M31, which form the basis for us to analyze the variation of RSGs.

The variation is analyzed with the time-series data taken by the iPTF survey, which spans about 2000 days. From the CCD images, the differential photometry is performed to all the RSGs with the SExtractor tool by making the average of all RSGs as the reference star, which achieves an accuracy of about 0.04 mag. The light curve is then fitted by the PDM, GLS, DFT, and WWZ methods, and a period is considered to be real only when it is identified by at least two methods for RSGs with semi-regular variation. Based on the characteristics of light curves, RSGs are classified into semi-regular variables, variables with LSP, irregular variables, and others. In total, 84 RSGs in M33 and 56 RSGs in M31 are found to show semi-regular variation, in which 19 stars in M33 and 7 stars in M31 are identified in the first overtone mode and are excluded for the P–L analysis. We take 65 RSGs in M33 and 49 RSGs in M31 to analyze the P–L relation in visual, near-infrared, and mid-infrared bands.

The P–L relation exists in all the infrared bands. In particular, the relation is very tight in the 2MASS/JHK_S bands and the *Spitzer*/IRAC1-3 bands. In the *Spitzer*/IRAC [8.0] and *Spitzer*/MIPS [24] bands, the P–L relation is relatively sparse due to the emission of circumstellar dust. In the visual band, the P–L relation is not clear, which can be understood by inhomogeneous extinction. When the dereddening Wesenheit index $W_{BV} = V - R_V(B - V)$ is taken into account, the P–L relation shows up, although it is not as tight as in the infrared bands.

The results are compared with the P–L relations of RSGs in other galaxies, i.e., the SMC, the LMC and the Milky Way. The P–L relation in K band in these galaxies are found to be similar, showing no apparent dependence on the metallicity.

From the P–L relation, the pulsation mode of RSGs in the M33 and M31 is compared with the theoretical model and is found to be very possibly in the fundamental pulsation mode. When compared with the SMC, LMC and Galaxy, it seems that the pulsation mode shows dependence on the metallicity. This phenomenon may be related to convection and its dependence on metallicity and deserves further investigation.

Due to the limitations of the iPTF data available at now, the LSP of RSGs cannot be determined with reasonable accuracy. We may obtain long baseline data from the combination of the iPTF data and the Panoramic Survey Telescope and Rapid Response System (Pan-STARRS) DR2 data to determine the LSP in the future.

We thank Prof. Yan Li for helpful discussions. Special thanks go to the anonymous referee for their very helpful suggestions, which improved the paper significantly. This work is supported by NSFC through Projects 11533002 and U1631104. This work made use of the data taken by *LGGS*, iPTF, 2MASS, and *Spitzer*. This work made use of PyAstronomy.

Software: astropy (Astropy Collaboration et al. 2013), SExtractor (Bertin & Arnouts 1996), VARTOOLS (Hartman & Bakos 2016).

ORCID iDs

Bi-Wei Jiang https://orcid.org/0000-0003-3168-2617
Ming Yang https://orcid.org/0000-0001-8247-4936
Jian Gao https://orcid.org/0000-0003-4195-0195

References

Alcock, C., Allsman, R. A., Alves, D., et al. 1997, ApJ, 486, 697
Astropy Collaboration, Robitaille, T. P., Tollerud, E. J., et al. 2013, A&A, 558, A33
Bertin, E., & Arnouts, S. 1996, A&AS, 117, 393
Bessell, M. S., Castelli, F., & Plez, B. 1998a, A&A, 333, 231
Bessell, M. S., Castelli, F., & Plez, B. 1998b, A&A, 337, 321
Bhardwaj, A., Kanbur, S. M., Marconi, M., et al. 2017, MNRAS, 466, 2805
Brunish, W. M., Gallagher, J. S., & Truran, J. W. 1986, AJ, 91, 598
Cardelli, J. A., Clayton, G. C., & Mathis, J. S. 1989, ApJ, 345, 245
Chun, S., Yoon, S., Jung, M., Kim, D. U., & Kim, J. 2018, ApJ, 853, 79
Clayton, G. C., Gordon, K. D., Bianchi, L. C., et al. 2015, ApJ, 815, 14
Dong, H., Li, Z., Wang, Q. D., et al. 2014, ApJ, 785, 136
Dorda, R., Negueruela, I., González-Fernández, C., & Tabernero, H. M. 2016, A&A, 592, 16
Drout, M. R., Massey, P., & Meynet, G. 2012, ApJ, 750, 97
Ekström, S., Georgy, C., Eggenberger, P., et al. 2012, A&A, 537, 146
Elias, J. H., Frogel, J. A., & Humphreys, R. M. 1985, ApJS, 57, 91
Esteban, C., & Peimbert, M. 1995, MxAC, 3, 133
Foster, G. 1996, AJ, 112, 1709
Gaia Collaboration, Brown, A. G., Vallenari, A., et al. 2018, A&A, 616, 1
Garnett, D. R., Shields, G. A., Skillman, E. D., Sagan, S. P., & Dufour, R. J. 1997, ApJ, 489, 63
Guo, J. H., & Li, Y. 2002, ApJ, 565, 559
Hartman, J. D., & Bakos, G. A. 2016, A&C, 17, 1
Hog, E., Kuzmin, A., Bastian, U., et al. 1998, A&A, 335, 65
Hughes, S. M. G., & Wood, P. R. 1990, AJ, 99, 784
Josselin, E., Blommaert, J. A. D. L., Groenewegen, M. A. T., Omont, A., & Li, F. L. 2000, A&A, 357, 225
Kinman, T. D., Mould, J. R., & Wood, P. R. 1987, AJ, 93, 833
Kiss, L. L., Szabó, Gy. M., Bedding, T. R., et al. 2006, MNRAS, 372, 1721
Kudritzki, R-P., & Reimers, D. 1978, A&A, 70, 227
Law, N. M., Kulkarni, S. R., Dekany, R. G., et al. 2009, PASP, 121, 1395
Levesque, E. M., & Massey, P. 2012, AJ, 144, 2
Levesque, E. M., Massey, P., Olsen, K. A. G., et al. 2005, ApJ, 628, 973
Levesque, E. M., Massey, P., Olsen, K. A. G., & Plez, B. 2007, ApJ, 667, 202
Lomb, N. R. 1976, ApSS, 39, 447
Maeder, A., Lequeux, J., & Azzopardi, M. 1980, A&A, 90, L17
Massey, P. 1998, ApJ, 501, 153
Massey, P. 2002, ApJS, 141, 81
Massey, P., & Evans, K. A. 2016, ApJ, 826, 224
Massey, P., Levesque, E. M., Plez, B., & Olsen, K. A. G. 2008, in IAU Symp. 250, Massive Stars as Cosmic Engines, ed. F. Bresolin, P. A. Crowther, & J. Puls (Cambridge: Cambridge Univ. Press), 97
Massey, P., Neugent, K. F., & Smart, B. M. 2016, AJ, 152, 62
Massey, P., Olsen, K. A., Hodge, P. W., et al. 2006, AJ, 131, 2478
Massey, P., & Olsen, K. A. G. 2003, AJ, 126, 2867
Massey, P., Olsen, K. A. G., Hodge, P. W., et al. 2007, AJ, 133, 2393
Massey, P., Silva, D. R., Levesque, E. M., et al. 2009, ApJ, 703, 420
Maund, J. R. 2017, MNRAS, 469, 2202
Mauron, N., & Josselin, E. 2011, A&A, 526, 156
Orosz, J. A., Mcclintock, J. E., Narayan, R., et al. 2007, Natur, 449, 872
Paxton, B., Bildsten, L., Dotter, A., et al. 2011, ApJS, 192, 3
Paxton, B., Cantiello, M., Arras, P., et al. 2013, ApJS, 208, 4
Paxton, B., Marchant, P., Schwab, J., et al. 2015, ApJS, 220, 15
Paxton, B., Schwab, J., Bauer, E. B., et al. 2018, ApJS, 234, 34
Perina, S., Federici, L., Bellazzini, M., et al. 2009, A&A, 507, 1375
Pojmanski, G. 2002, AcA, 52, 397
Rau, A., Kulkarni, S. R., Law, N. M., et al. 2009, PASP, 121, 1334
Reimers, D. 1975, MSRSL, 8, 369
Riechers, D. A., Bradford, C. M., Clements, D. L., et al. 2013, Natur, 496, 329
Robin, A. C., Reylé, C., Derrière, S., & Picaud, S. 2003, A&A, 409, 523
Rubin, V. C., & Ford, W. K. J. 1970, ApJ, 159, 379
Russell, S. C., & Dopita, M. C. 1990, ApJS, 74, 93
Salvatier, J., Wiecki, T., & Fonnesbeck, C. 2016, PeerJ Comp. Sci., 2, e55
Scargle, J. D. 1982, ApJ, 263, 835
Smartt, S. 2015, PASA, 32, 16
Smartt, S. J., Eldridge, J. J., Crockett, R. M., & Maund, J. R. 2009, MNRAS, 395, 1409
Smith, H., Jr., & Eichhorn, H. 1996, MNRAS, 281, 211
Soraisam, M. D., Bildsten, L., Drout, M. R., et al. 2018, ApJ, 859, 73
Stellingwerf, R. F. 1978, ApJ, 224, 953
Stothers, R., & Leung, K. C. 1971, A&A, 10, 290
Stothers, R. B., & Chin, C-W. 1996, ApJ, 468, 842
Tammann, G. A., Sandage, A., & Reindl, B. 2003, A&A, 404, 423

van Loon, J. Th., Cioni, M.-R. L., Zijlstra, A. A., & Loup, C. 2005, A&A, 438, 273
Verhoelst, T., Der Zypen, N. V., Hony, S., et al. 2009, A&A, 498, 127
Wang, S., & Jiang, B. W. 2014, ApJL, 788, 32
Yang, M., Bonanos, A. Z., Jiang, B. W., et al. 2018, A&A, 616, 175
Yang, M., & Jiang, B. W. 2011, ApJ, 727, 53
Yang, M., & Jiang, B. W. 2012, ApJ, 754, 35
Yecko, P. A., Kollath, Z., & Buchler, J. R. 1998, A&A, 336, 553
Zaritsky, D., Kennicutt, R. C., Jr., & Huchra, J. P. 1994, ApJ, 420, 87
Zechmeister, M., & Kurster, M. 2009, A&A, 496, 577